RESEARCH ARTICLE

Activation of Fe species on graphitic carbon nitride nanotubes for efficient photocatalytic ammonia synthesis

Zhao Mo[1] | Keqiang Xu[2] | Limin Yu[1] | Tianyu Huang[3] | Yanhua Song[4] | Junjie Yuan[1] | Cheng Ding[2] | Yucheng Lei[1] | Huaming Li[1] | Hui Xu[1] (ORCID)

[1]School of Materials Science & Engineering, Institute for Energy Research, Jiangsu University, Zhenjiang, P. R. China

[2]Key Laboratory for Advanced Technology in Environmental Protection of Jiangsu Province, Yancheng Institute of Technology, Yancheng, P. R. China

[3]China Construction Eighth Engineering Division Corp., LTD, Shanghai, P. R. China

[4]School of Environmental and Chemical Engineering, Jiangsu University of Science and Technology, Zhenjiang, P. R. China

Correspondence
Yucheng Lei and Hui Xu, School of Materials Science & Engineering, Institute for Energy Research, Jiangsu University, Zhenjiang 212013, P. R. China.
Email: yclei@ujs.edu.cn; xh@ujs.edu.cn

Summary
Photocatalytic ammonia synthesis, as a suitable alternative to traditional Haber-Bosch artificial nitrogen reduction process, has aroused widespread interest. Graphitic carbon nitride ($g-C_3N_4$) has emerged as an attractive metal-free photocatalyst, but its development in photocatalytic ammonia synthesis field is greatly shackled to the low photocatalytic activity. In this work, a highly active Fe-doped tubular graphitic carbon nitride (Fe-TCN) is reported, which demonstrates transformative performance on photosynthesis of NH_3 from N_2. Such excellent photocatalytic activity is derived from the incorporation of Fe species as the active sites to efficiently adsorb and activate N_2 molecules on the surface of TCN. Simultaneously, surface-active Fe species are also regarded as the trap sites of electrons, and the concentrated electrons at surface-active Fe species can significantly improve the NH_3 conversion efficiency. Impressively, Fe-TCN realized a 9.5-fold enhancement of NH_3 production rate with the yield of 647 μmol g^{-1} h^{-1} ($\lambda \geq 420$ nm), and the corresponding reaction pathways are also established.

KEYWORDS
ammonia synthesis, carbon nitride, Fe doping, Photocatalysis

1 | INTRODUCTION

Ammonia (NH_3) is the essential for the building of life and the ingredient or intermediate of many chemicals such as fertilizer and drugs.[1,2] Nitrogen fixation widely exists in nature through either nitrogenase or thunder and lightning to convert N_2 to NH_3.[3] However, the NH_3 produced by nature cannot meet the demand in human society. To solve the problem, N_2 can be reduced to NH_3 via industrial Haber-Bosch process, which requires severe condition including high pressure (15-25 MPa), high temperature (300-500°C), consuming 5% natural gas and discharging hundreds of millions of tons about carbon dioxide (CO_2) every year.[4] Therefore, it is crucial to explore an energy-saving nitrogen fixation process under mild condition to replace the traditional high energy-consuming of Haber-Bosch process.[5] In thermodynamics, the reaction can spontaneously act, since the Gibbs free energy of nitrogen fixation is less than zero. However, the reaction kinetics is sluggish due to the high dissociation energy of $N \equiv N$ triple bond (941 kJ mol^{-1}).[6] Normally, there are two mechanisms for nitrogen fixation: dissociative mechanism and associative mechanism.[2] A typical example of dissociative mechanism is Haber-Bosch process. The $N \equiv N$ bond breaks into nitrogen atoms which are adsorbed on the substrate and afterwards hydrogenated to produce NH_3.[7] It requires a lot of energy to open the $N \equiv N$ bond, causing that the reaction condition is harsh in Haber-Bosch process.[8] The photocatalytic process chooses associative mechanism to achieve nitrogen fixation, which requires much less energy investment.[9] Typically, two pathways are included in this catalogue which are distal associative avenue and alternating avenue. On the first avenue, the hydrogenation reaction is carried out on one side of $N \equiv N$ molecule continuously until NH_3 is generated and released, and the same procedure is subsequently implemented on the other side of $N \equiv N$ molecule. But on the alternating avenue, the hydrogenation reaction is alternately carried out on the two nitrogen atoms.[10]

Photocatalytic nitrogen fixation reaction is of great concern as an alternation for traditional Haber-Bosch process since the Schrauzer and Guth found that TiO_2 with iron (Fe) doping can achieve nitrogen fixation under a mild condition in 1977.[11,12] NH_3 is synthesized from N_2 and water with solar light as driving force under room temperature and normal pressure in a perfect photocatalytic nitrogen fixation model.[13] Up to now, researchers have proved that miscellaneous catalysts can be used for the reaction with sacrifice agent added or not, including TiO_2/Au nanorods, edge-rich black phosphorus nanoflakes, In_2O_3/In_2S_3 microsphere and so on.[14] However, the efficient absorption and activation of N_2 has always been the bottleneck.[15] Many methods are applied

to tackle with the challenge, such as heterojunction tuning and defect engineering.[16,17] Therein doping approach is a promising technology to deal with the problem mentioned above.[18] With heteroatoms doped, there is disturbance both to the electron structure and electronic density. At the same time, many defects on the surface of catalysts may facilitate the adsorption and activation of N_2, therefore the nitrogen fixation efficiency getting improved.[19]

Fe plays a vital role in both nitrogenase nitrogen fixation and industry NH_3 production.[20] From the recent study of nitrogenase structure, the active center of catalysis is the multi-iron metallocluster (Fe_3(II) Fe_4(III) M(III)), where M represents Mo, V, and Fe, in which N_2 is bond on the Fe^{2+} belt.[21] Chen et al. proposes that oxygen vacancies can be introduced through Fe doping, which increase current density and boost transfer of photogenerated carriers, therefore the nitrogen fixation efficiency getting improved.[22] Besides, graphitic carbon nitride (g-C_3N_4) has been the hot material for the photocatalytic reaction due to its low-cost, easy access and tunable band level.[23,24] As a star semiconductor, a wide range of light can be adsorbed owing to its narrow band gap. Moreover, many kinds of morphology are prepared which show many unique properties. From Jiang's group, g-C_3N_4 nanotubes with upconversion nanoparticles are prepared, which extend the light adsorption region from UV region to near-infrared region and inhabit the recombination of photogenerated carriers, thus enhancing the photocatalytic nitrogen fixation efficiency.[25]

Herein, a Fe-doped tubular graphitic carbon nitride (Fe-TCN) for photocatalytic ammonia synthesis was prepared by a simple in-situ growth method. It is demonstrated that surface-active Fe species can serve as a multifunctional center to adsorb and activate N_2. Simultaneously, surface-active Fe species can also boost the transfer of photoinduced electrons from the catalyst surface to N_2, and the electron density change originated from Fe doping is beneficial to the separation between photoexcited electrons and holes. The optimal Fe(0.015)-TCN showed outstanding nitrogen fixation efficiency (647 μmol g^{-1} h^{-1}). This work provides an effective method for designing a reaction system with high-efficiency photocatalytic NH_3 synthesis, and also broadens the application of carbon nitride materials in the field of photocatalytic NH_3 synthesis.

2 | EXPERIMENT

2.1 | Materials

Melamine, hydroxylammonium chloride, and potassium ferrate were purchased from Sinopharm Chemical

Reagent Co., Ltd. Potassium sodium tartrate and Nessler's reagent were purchased from Pinggen, Guangdong. Deionized water was prepared from Ultra-pure water in laboratory. All chemicals were used without any further purification.

2.2 | Synthesis of Samples

The TCN was prepared according to our previous work.[26] Firstly, the intermediate of Fe-TCN was prepared by hydrothermal method. Melamine, hydroxylammonium chloride, a certain amount of potassium ferrate and deionized water were added into the 50 ml high pressure reactor lined with tetrafluoroethylene, followed by magnetic stirring treatment for 30 min and then being kept at 120°C for 12 h. Afterwards, the resultant suspension was separated via centrifugation followed by wash for several times with deionized water and ethanol. After drying for 12 h at 80°C, the yellow light powder obtained was calcined at 500°C for 4 h in a crucible wrapped by a lid and labeled as Fe(x)-TCN (x represents the mass of added potassium ferrate, equals to 0, 0.005 g, 0.015 g, 0.025 g) (Scheme 1). To obtain bulk g-C_3N_4, 2 g melamine was put into a crucible with a cover and heated at 550°C for 4 h with a heating rate of 2°C/min in a muffle furnace. The obtained sample was ground into a powder for later use.

2.3 | Characterization

Scanning electron microscopy (SEM) images were acquired on a JSM-7001F field-emission microscope (JEOL, Japan). Transmission electron microscopy (TEM) images were carried out on a JEOL-JEM-2010

transmission electron microscopy (JEOL, Japan) at 200 kV. X-ray diffraction (XRD) patterns were collected on a Bruker D8 diffractometer using Cu Kα radiation (λ = 1.5418 Å, 2θ = 10-80°). Fourier Transform Infrared Spectroscopy (FT-IR) spectra were performed on IS50 FT-IR of Thermo Nicolet with the standard KBr disk method. Diffuse reflectance spectroscopy (DRS) spectra were obtained from a Shimadzu UV-3600 spectrometer (Shimadzu, Japan) with $BaSO_4$ as a reference. X-ray photoelectron spectroscopy (XPS) spectra were gained on an ESCA Lab MKII. Transient photocurrent (TPC) and electrochemical impedance spectroscopy (EIS) measurements were carried out on CHI660B electrochemical station (Chen Hua, Shanghai, China) with a platinum wire as the counter electrode, Ag/AgCl (in saturated KCl) as a reference electrode and phosphate buffer (PBS) (0.1 M, pH = 7.0) as the electrolyte. Thereinto, a 500 W Xe arc lamp was used as a light source. The dispersion was prepared by 1 mg sample powder uniformly dispersed in 1 mL deionized water, and 20 μL of the resulting colloidal dispersion (1 mg/mL) was added dropwise onto a piece of indium tin oxide (ITO) with the fixed area of 1*0.5 cm and dried on air dry oven.

2.4 | Measurement of photocatalytic ammonia synthesis

The photocatalytic performance of the prepared samples was evaluated by the photocatalytic nitrogen fixation reaction under irradiation with an optical filter (λ ≥ 420 nm). 20 mg catalysts were dispersed into 50 mL methanol solution (1/100 vol%) which were put into a custom photoreaction cell. Then high purity N_2 was bubbled into the mixture for 30 min and sealed the air vent when it was over. Put the photoreaction cell on a
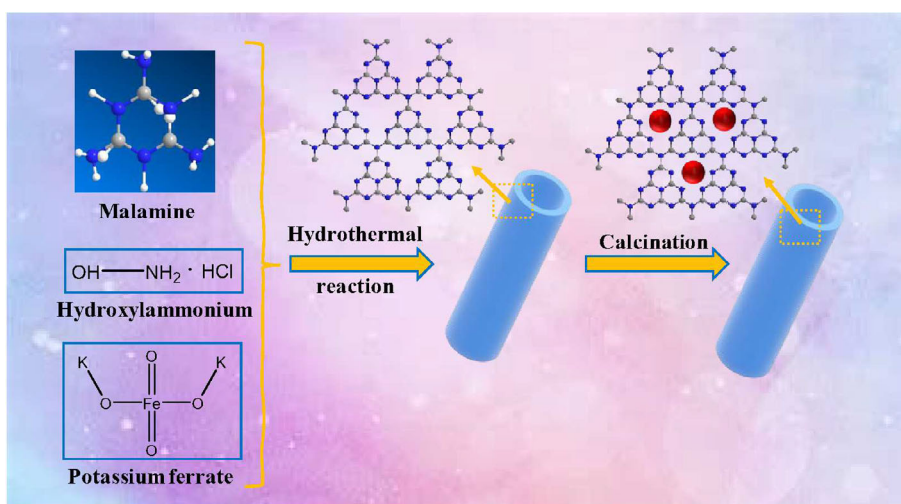
SCHEME 1 Synthetic route of Fe-TCN via two step preparation method

magnetic stirrer and keep it stirring. Circulating cooling water was connected and controlled at ~25°C. Withdraw the first sample after 30 min dark reaction. Then the light (300 W, High uniformity integrated Xenon light source, PLS-FX300HU, Beijing Perfectlight) was turned on, and one sample was taken every 30 min until 6 samples are taken.

The ammonia yield was measured by Nessler's reagent colorimetric method which was well adapted to this reaction system. Firstly, a set of standard concentration gradients was configured (0 μg, 1 μg, 2 μg, 4 μg, 8 μg, 12 μg, 16 μg, 20 μg Nessler's reagents were added into 10 mL colorimetric cylinder). Secondly, 200 μL potassium sodium tartrate and 200 μL Nessler's reagent in sequence were added into this tube, and its absorbance at 420 nm after 10-15 min were measured when it was fully developed. Finally, a standard curve can be fit when pictured using absorbance as the ordinate and ammonia content as the abscissa. The test method for the nitrogen content of the catalyst for nitrogen fixation refers to the standard curve drawing method, and the sample was replaced with the reaction liquid to make sure the accuracy of colorimetric method.

3 | RESULTS AND DISCUSSION

On designing the optimized photocatalytic nitrogen fixation system with surface-active Fe species modification, the photocatalytic nitrogen reduction is assessed under visible light irradiation ($\lambda \geq 420$ nm). As shown in Figure 1A, the NH_3 production rates of bulk g-C_3N_4, Fe(0)-TCN, Fe(0.005)-TCN, Fe(0.015)-TCN and Fe(0.025)-TCN are 68, 277, 353, 647, 515 μmol g^{-1} h^{-1}. The enhancement of NH_3 yield demonstrates that the introduction of moderate active Fe species promotes the nitrogen fixation reaction. As the content of active Fe species increases to 0.025, the nitrogen fixation rate falls because the excess Fe species of Fe-TCN may form the recombination sites of photoinduced electrons-holes pairs.[27] In addition, the photocatalytic performance of this work seems to be higher than some of CN-based photocatalysts for photocatalytic nitrogen fixation (Table S1). To exclude the possible nitrogen contaminations from the photocatalyst or experiment process, the high purity N_2 is bubbled into reaction solution before each photocatalytic experiment.[28,29] UV-vis DRS spectra are further used to measure the concentration of NO_3^- before and after photocatalytic experiment (Figure S1), the results suggest that almost no NO_3^- exists in the reaction solution.[29] Next, a series of control experiments are carried out to study the origin of generated NH_3 production. When the performance is evaluated under Ar atmosphere, no obvious ammonia is detected (Figure 1B), which rules out the impact of possible nitrogen contaminations from the reaction solution, indicating that the nitrogen of as-synthesized NH_3 originates from N_2.[30] The control experiment without light or methanol as sacrifice agent is carried out at the same time. It turns out that light and sacrifice agent are indispensable for the process
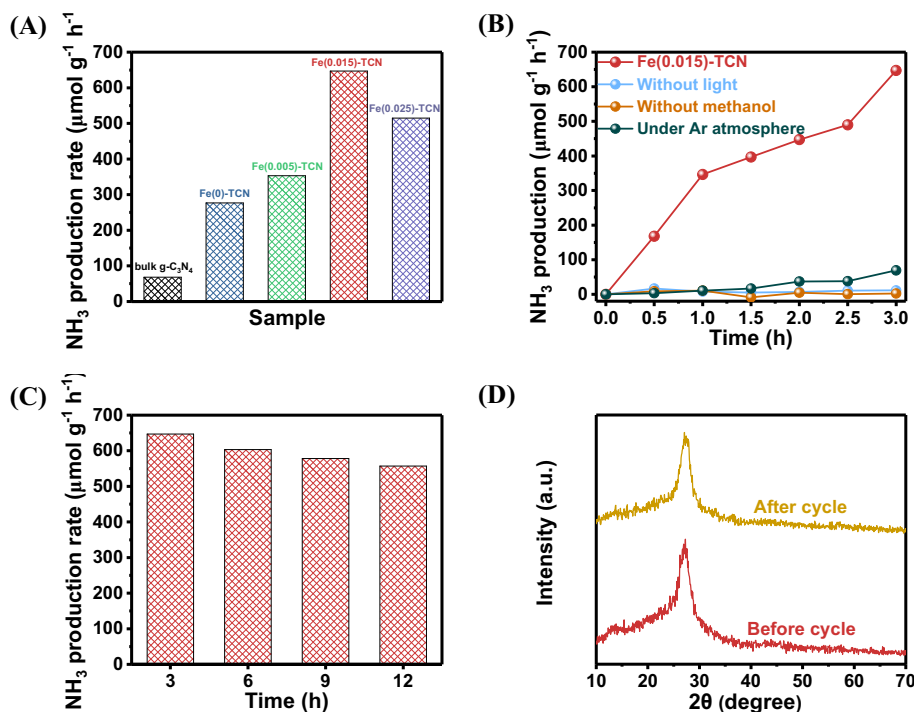

FIGURE 1 (A) Photocatalytic ammonia synthesis over bulk g-C_3N_4, Fe(0)-TCN, Fe(0.005)-TCN, Fe(0.015)-TCN, and Fe(0.025)-TCN; (B) Photocatalytic ammonia synthesis over Fe(0.015)-TCN under Ar atmosphere, or without methanol, or without light; (C) Stability test; (D) XRD patterns of Fe(0.015)-TCN before and after the cycling photocatalytic experiments

since the observed NH_3 is negligible. Above all, the detected NH_3 production really originates from the photocatalytic nitrogen reduction over Fe-TCN. Afterwards, the steady ability of Fe(0.015)-TCN is measured. As shown in Figure 1C, the NH_3 production rate is only slightly attenuated, which may be attributed to the generated intermediates covering on the surface of substance that impede the release of photocatalytic outcome NH_3.[31] Fe(0.015)-TCN is further characterized by XRD after the photocatalytic reaction (Figure 1D), the results reveal that the structure of g-C_3N_4 is unchanged, confirming that Fe(0.015)-TCN possesses a high photostability after a long period of photocatalytic reaction.[32,33]

The morphology of Fe(0.015)-TCN is characterized through SEM and TEM. After hydrothermal reaction and calcination, the Fe(0)-TCN shows nanotube shape (Figure 2B) differing from agminated block structure of bulk g-C_3N_4 (Figure 2A). From Figure 2C,D, it is clear that the synthesized Fe(0.015)-TCN with diameter of 200 nm around, and many holes distribute on it evenly, which indicates fast transport speed of photogenerated electrons.[34] And no Fe compound is observed, indicating Fe does not exist in the nanotube CN in compound form but in another way. To further explore the structure of Fe-TCN, XRD and FT-IR are employed. From XRD patterns (Figure 3A), there is a peak at 27.3° in bulk g-C_3N_4, Fe(0)-TCN and Fe(0.015)-TCN, which is assigned to the interlayer stacking of g-C_3N_4, corresponding to (002) lattice plane. Significantly, the peaks of Fe-TCN become weaker and wider than that of bulk g-C_3N_4, probably because the incorporation of surface-active Fe species influences the original order of g-C_3N_4, and then result in

the expansion of interplanar spacing.[35] Similarly, no obvious difference is presented on FT-IR spectra (Figure 3B). Specifically, the characteristic peak locates at $814\ cm^{-1}$, corresponding to breathing mode of s-triazine units.[36] Peaks in the range from $1240\ cm^{-1}$ to $1640\ cm^{-1}$ are ascribed to CN heterocycles.[37,38] And peaks between $2968\ cm^{-1}$ to $3426\ cm^{-1}$ are originated from non-condensing amino groups and the adsorbed H_2O molecules.[39]

In addition, XPS spectra can analyze the chemical composition and chemical bonding of the material.[40] As shown in Figure 4A, the material contains C, N, Fe, O, and other elements, which can prove that active Fe species are indeed doped into the carbon nitride material. As shown in Figure 4B, the C 1 s peak of the material is divided into three peaks. The peaks at 284.8 eV and 287.6 eV correspond to C-C bonds or C=C bonds and N-C=N bonds, respectively.[41] However, with the addition of active Fe species, the peak at 287.6 eV is blue-shifted, indicating that Fe and N may form Fe-N bonds, thereby reducing the electron density of N atoms.[42] In addition, a new peak is observed at 286.2 eV, corresponding to C-O. This may be due to the loss of part of N atoms in Fe(0.015)-TCN, which changes the electron density of C-N and improves the N_2 adsorption performance of catalyst.[8] As shown in Figure 4C, three peaks can be observed in the N 1 s spectrum of the catalyst, located at 398.1 eV, 399.1 eV and 400.5 eV, corresponding to C=N-C, N-CH_3 and C-N-H, respectively.[43] It is important to note that, the peaks of Fe(0.015)-TCN in the N 1 s spectrum shift to the higher binding energy, which may be due to the interaction between active Fe species and N
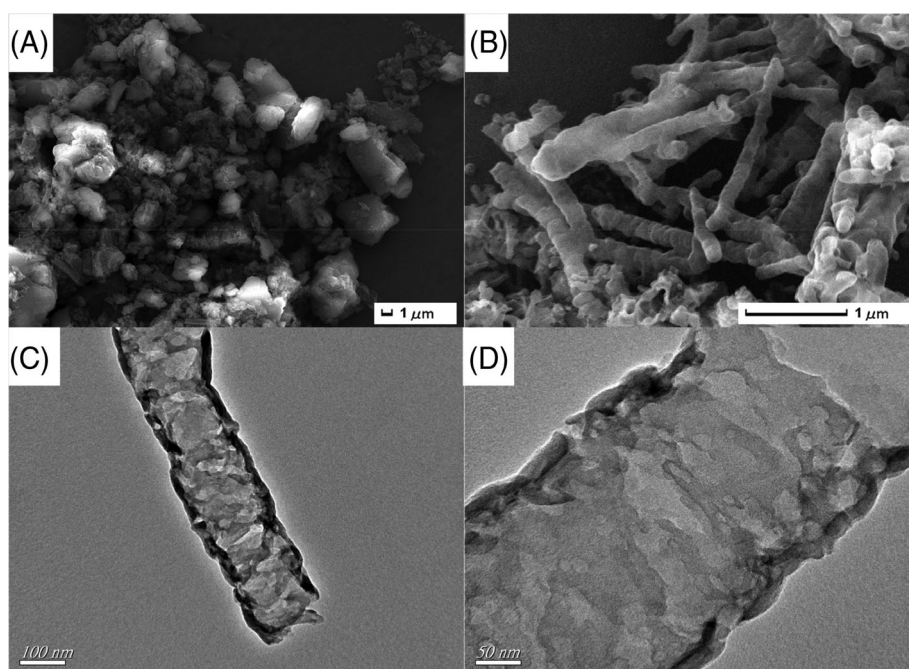

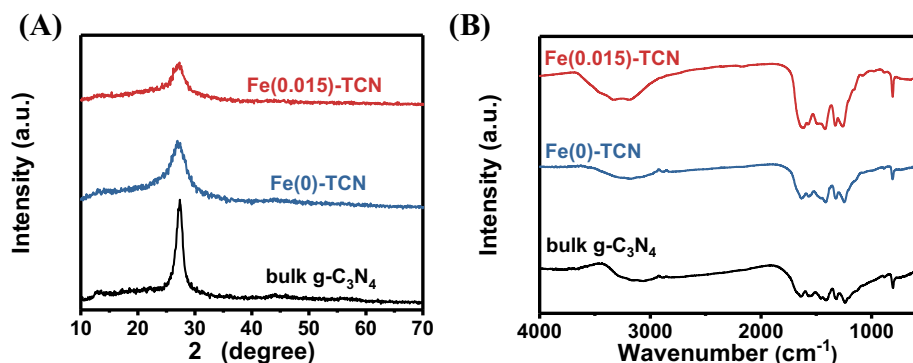**FIGURE 2** SEM images of (A) bulk g-C_3N_4, (B) Fe(0)-TCN; (C and D) TEM images of Fe(0.015)-TCN

FIGURE 3 (A) XRD patterns and (B) FT-IR spectra of bulk g-C_3N_4, Fe(0)-TCN and Fe(0.015)-TCN
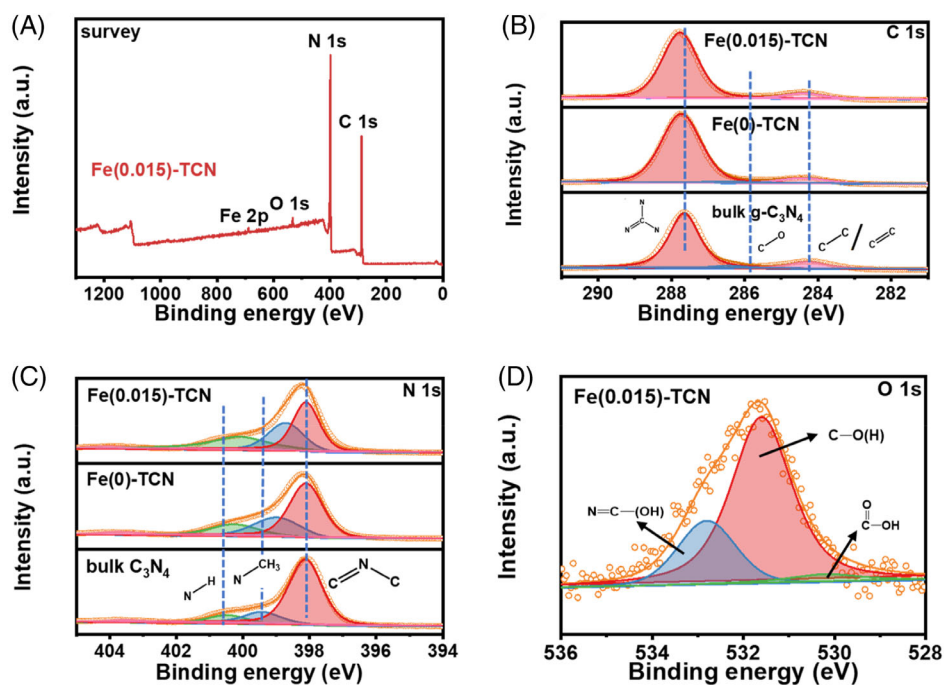

FIGURE 4 XPS spectra: (A) survey, (B) C 1 s, (C) N 1 s, and (D) O 1 s

atoms of g-C_3N_4.[43] In Figure 4D, it can be seen that the O 1 s spectrum of Fe(0.015)-TCN mainly shows three peaks, located at 530.1 eV, 531.6 eV, and 532.8 eV, which belong to O=C-OH, C-O(H), N=C-(OH).[44] In the high-resolution Fe 2p XPS spectrum of Fe(0.015)-TCN (Figure S2), two binding energy peaks at 711.9 and 725.1 eV are assigned to Fe $2p_{3/2}$ and Fe $2p_{1/2}$, respectively. The result is attributed to the existence of active Fe species on the surface of Fe-TCN.[45]

From the UV-vis DRS spectra (Figure 5A), a distinct blue shift of absorption edge was detected, which can be attributed to quantum confinement effect due to the nanoscale tube wall.[46] Furthermore, DRS and XPS were used to analyze the energy band structure of the material, as shown in Figure 5B-D and 6A, according to the Kubelka-Munk function plot, the bulk g-C_3N_4, Fe(0)-TCN and Fe(0.015)-TCN can be analyzed. The band gaps of the bulk g-C_3N_4, Fe(0)-TCN and Fe(0.015)-TCN are 2.76 eV, 2.95 eV, and 2.99 eV, which are consistent with

the DRS characterization results. The valence band (VB) values of the bulk g-C_3N_4, Fe(0)-TCN and Fe(0.015)-TCN can be calculated to be 1.76 eV, 2.01 eV, and 2.03 eV according to the VB XPS spectra (Figure 6A). According to the band gaps and VB values, the calculated conduction band (CB) values of the bulk g-C_3N_4, Fe(0)-TCN and Fe(0.015)-TCN can be −1.00 eV, −0.94 eV, and − 0.96 eV respectively. From this, the energy level structure diagram of the catalyst can be drawn, as shown in Figure 6B. It can be seen that the tubular structure significantly affects the energy band position of the material, and at the same time the VB positions of Fe(0)-TCN and Fe(0.015)-TCN are lifted, In addition, the doping of active Fe species also causes a change in the energy level structure of the material. The deeper VB position of Fe(0.015)-TCN has stronger oxidation capacity than that of bulk g-C_3N_4 and Fe(0)-TCN, which contributes to the oxidation reaction. In other words, this may improve the reduction reaction indirectly. Meanwhile, the Fe(0.015)-TCN

FIGURE 5 (A) UV–Vis DRS spectra of bulk g-C$_3$N$_4$, Fe(0)-TCN, and Fe(0.015)-TCN; Kubelka-Munk function vs photon energy curves: (B) bulk g-C$_3$N$_4$, (C) Fe(0)-TCN, and (D) Fe(0.015)-TCN
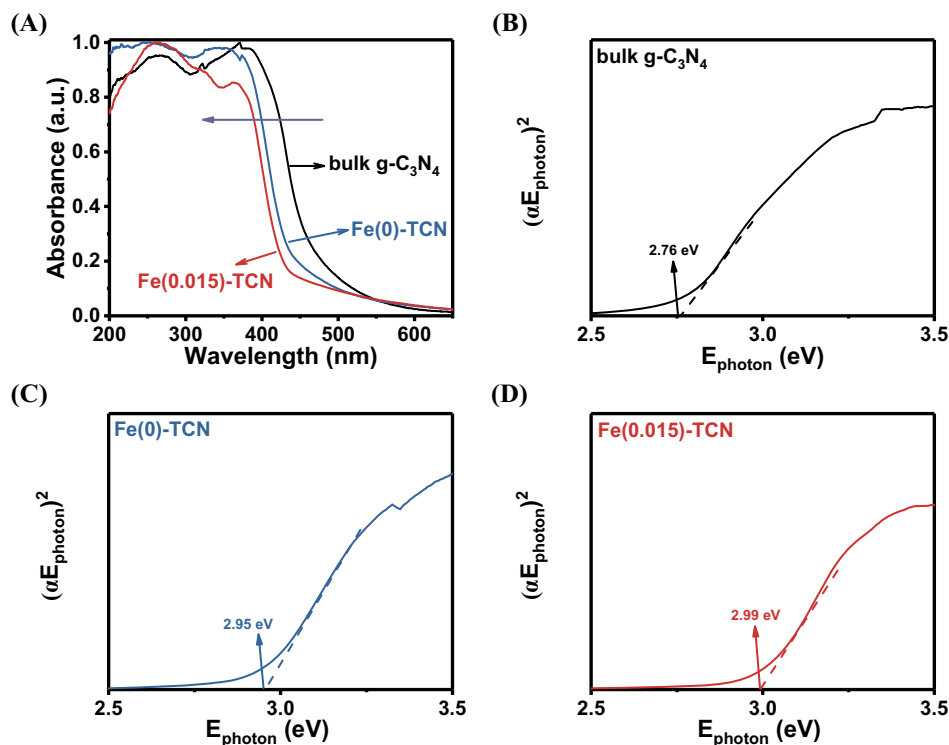
FIGURE 6 (A) VB XPS spectra and (B) energy band diagram of bulk g-C$_3$N$_4$, Fe(0)-TCN, and Fe(0.015)-TCN
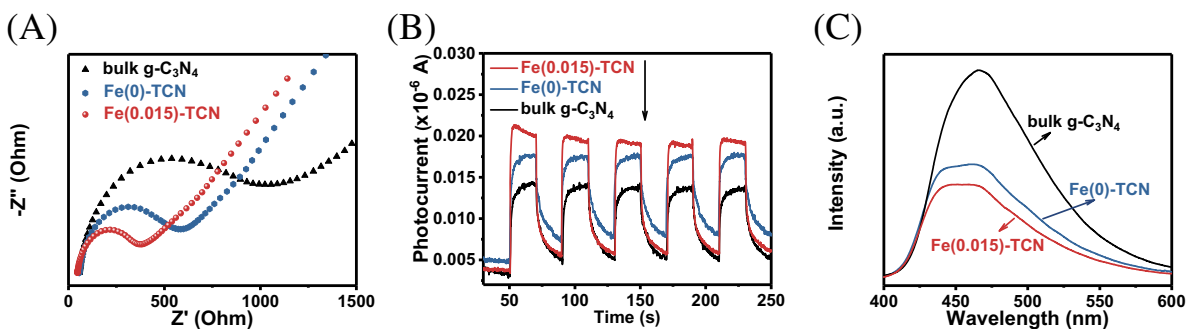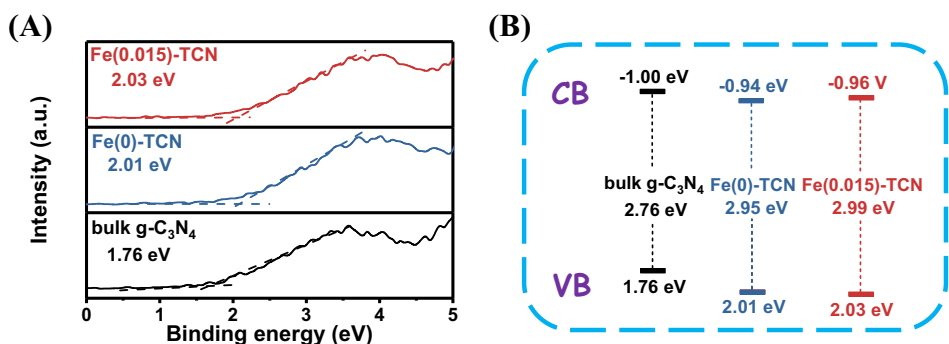
FIGURE 7 (A) EIS plots; (B) TPC curves and (C) PL emission spectra of bulk g-C$_3$N$_4$, Fe(0)-TCN, and Fe(0.015)-TCN

possesses the stronger reduction ability than that of Fe(0)-TCN due to the deeper CB level, which is good for N$_2$ reduction reaction.

To explore the mechanism of promoted photocatalytic nitrogen fixation reaction, EIS, TPC, and photoluminescence (PL) tests are carried out. Fe(0.015)-TCN shows a smaller radius in EIS plot (Figure 7A) and a higher photocurrent intensity (Figure 7B), which means a faster photogenerated electrons transport rate and the ability to inhibit the recombination of photoinduced carriers.[47,48] Besides, PL spectra are
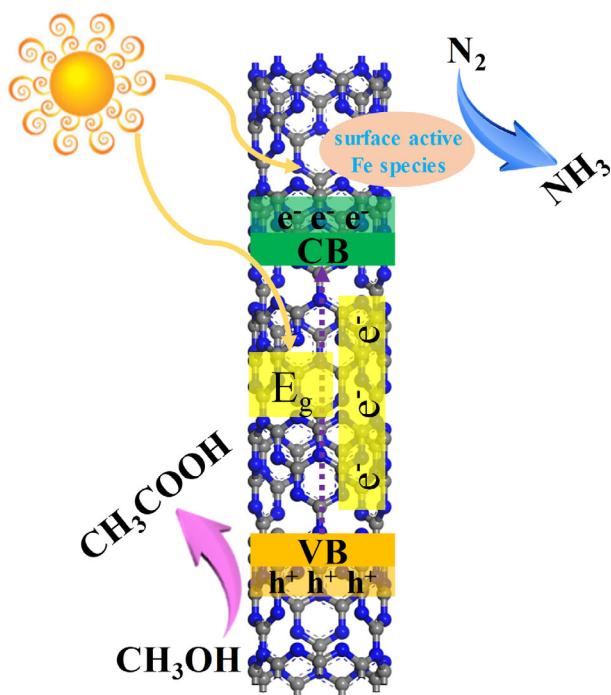
FIGURE 8 Photocatalytic ammonia synthesis mechanism of Fe-TCN

utilized to explore the separation efficiency of photoinduced electron-hole pairs. The steady state PL emission spectra are excited by 360 nm. The lower peak intensity of Fe(0.015)-TCN (Figure 7C) indicates that a higher separation efficiency of photogenerated pairs.[49,50] Therefore, a mechanism hypothesis is proposed. The Bode plots are presented in Figure S3, the peak of the phase angle curves represents the speed of the charge transfer at the interface between photocatalyst and ITO. The peak frequency of Fe(0.015)-TCN is obviously higher than that of bulk g-C_3N_4, indicating that the charge transfer is fastest between Fe(0.015)-TCN and ITO. As shown in Figure 8, under the irradiation of visible light, the photogenerated electron-hole pairs of Fe-TCN are separated, and the doped active Fe species serve as the active site to trap the excited electrons, adsorb and activate N_2, which is beneficial to boost the transportation of N_2 to NH_3.[16] Also, it is helpful to inhibit the recombination of photogenerated electron-hole pairs and enhance the electrons migration rate. Consequently, the photocatalytic nitrogen fixation rate is promoted. The concentrated electrons at the surface of active Fe species can participate in nitrogen reduction reaction, and the photoinduced holes can react with CH_3OH to form formic acid and other by-products.[51,52]

4 | CONCLUSION

In summary, this work successfully introduces active Fe species into TCN through the hydrothermal calcination method, effectively improving the photocatalytic nitrogen fixation performance of bulk g-C_3N_4. The porous nanotubular structure endows the material with strong light absorption, fast electrons migration capability and is beneficial to the regulation of the material's energy band structure. The doping of active Fe species does not cause change in the morphology of the catalyst. The introduction of active Fe species changes the electronic structure of g-C_3N_4, which can widen the VB and CB positions, resulting in an enhancement in redox ability. In addition, the doping of active Fe species can also enhance the adsorption capacity of N_2 and inhibits the recombination of photogenerated carriers. View from above, the photocatalytic activity of Fe-TCN is significantly improved, the corresponding NH_3 production rate is up to 647 mol g^{-1} h^{-1} ($\lambda \geq 420$ nm). This work provides a reference for photocatalytic ammonia synthesis based on the introduction of surface-active metal species in semiconductor.

DATA AVAILABILITY STATEMENT

The data that support the findings of this study are available from the corresponding author upon reasonable request.

ORCID

Hui Xu https://orcid.org/0000-0002-2823-5915

REFERENCES

1. Wu S, Chen Z, Yue W, et al. Single-atom high-Valent Fe(IV) for promoted photocatalytic nitrogen hydrogenation on porous TiO_2-SiO_2. *ACS Catal.* 2021;11:4362-4371.
2. Ye T, Park S, Lu Y, et al. Dissociative and associative concerted mechanism for ammonia synthesis over co-based catalyst. *J. Am. Chem. Soc.* 2021;143:12857-12866.
3. Zhao Z, Wang D, Gao R, et al. Magnetic-field-stimulated efficient photocatalytic N_2 fixation over defective $BaTiO_3$ perovskites. *Angew. Chem. Int. Ed.* 2021;60:11910-11918.

4. Bo Y, Wang H, Lin Y, et al. Altering hydrogenation pathways in photocatalytic nitrogen fixation by tuning local electronic structure of oxygen vacancy with dopant. *Angew. Chem. Int. Ed.* 2021;60:16085-16092.

5. Wang W, Zhou H, Liu Y, et al. Formation of BNC coordination to stabilize the exposed active nitrogen atoms in g-C_3N_4 for dramatically enhanced photocatalytic ammonia synthesis performance. *Small.* 2020;16:1906880.

6. Wu H, Li X, Cheng Y, et al. Plasmon-driven N_2 photofixation in pure water over MoO_{3-x} nanosheets under visible to NIR excitation. *J. Mater. Chem. A.* 2020;8:2827-2835.

7. Zhang G, Li Y, He C, Ren X, Zhang P, Mi H. Recent Progress in 2D catalysts for photocatalytic and Electrocatalytic artificial nitrogen reduction to ammonia. *Adv. Energy Mater.* 2021;11:2003294.

8. Shi L, Yin Y, Wang S, Sun H. Rational catalyst design for N_2 reduction under ambient conditions: strategies toward enhanced conversion efficiency. *ACS Catal.* 2020;10:6870-6899.

9. Li J, Liu P, Tang Y, et al. Single-atom Pt-N_3 sites on the stable covalent Triazine framework Nanosheets for photocatalytic N_2 fixation. *ACS Catal.* 2020;10:2431-2442.

10. Xiong J, Song P, Di J, Li H. Atomic-level active sites steering in ultrathin photocatalysts to trigger high efficiency nitrogen fixation. *Chem. Eng. J.* 2020;402:126208.

11. Huang Y, Zhang N, Wu Z, Xie X. Artificial nitrogen fixation over bismuth-based photocatalysts: fundamentals and future perspectives. *J. Mater. Chem. A.* 2020;8:4978-4995.

12. Li Q, Shen P, Tian Y, Li X, Chu K. Metal-free BN quantum dots/graphitic C_3N_4 heterostructure for nitrogen reduction reaction. *J. Colloid. Interface Sci.* 2022;606:204-212.

13. Zhang Y, Hou T, Xu Q, et al. Dual-metal sites boosting polarization of nitrogen molecules for efficient nitrogen Photofixation. *Adv. Sci.* 2021;8:2100302.

14. Wang T, Feng C, Liu J, et al. Bi_2WO_6 hollow microspheres with high specific surface area and oxygen vacancies for efficient photocatalysis N_2 fixation. *Chem. Eng. J.* 2021;414:128827.

15. Li P, Zhou Z, Wang Q, et al. Visible-light-driven nitrogen fixation catalyzed by Bi_5O_7Br nanostructures: enhanced performance by oxygen vacancies. *J. Am. Chem. Soc.* 2020;142:12430-12439.

16. Yang J, Bai H, Guo Y, et al. Photodriven disproportionation of nitrogen and its change to reductive nitrogen Photofixation. *Angew. Chem. Int. Ed.* 2021;60:927-936.

17. Zhao Y, Zheng L, Shi R, et al. Alkali etching of layered double hydroxide Nanosheets for enhanced photocatalytic N_2 reduction to NH_3. *Adv. Energy Mater.* 2020;10:2002199.

18. Zhang N, Li L, Shao Q, Zhu T, Huang X, Xiao X. Fe-doped BiOCl Nanosheets with light-switchable oxygen vacancies for photocatalytic nitrogen fixation. *ACS Appl. Energy Mater.* 2019;2:8394-8398.

19. Yang C, Zhu Y, Liu J, et al. Defect engineering for electrochemical nitrogen reduction reaction to ammonia. *Nano Energy.* 2020;77:105126.

20. Fang Y, Xue Y, Hui L, Yu H, Li Y. Graphdiyne@Janus magnetite for photocatalytic nitrogen fixation. *Angew Chem Int Ed.* 2021;60:3170-3174.

21. Vu M, Nguyen C, Do T. Synergistic effect of Fe doping and Plasmonic Au nanoparticles on $W_{18}O_{49}$ Nanorods for enhancing Photoelectrochemical nitrogen reduction. *ACS Sustainable Chem Eng.* 2020;8:12321-12330.

22. Chen X, Zhang X, Li Y, et al. Transition metal doping BiOBr nanosheets with oxygen vacancy and exposed {102} facets for visible light nitrogen fixation. *Appl Catal B Environ.* 2021;281:119516.

23. Mo Z, Di J, Yan P, et al. An all-organic D-A system for visible-light-driven overall water splitting. *Small.* 2020;16:2003914.

24. Zhu C, Xian Q, He Q, et al. Edge-rich Bicrystalline 1T/2H-MoS_2 Cocatalyst-decorated {110} terminated CeO_2 Nanorods for photocatalytic hydrogen evolution. *ACS Appl. Mater. Interfaces.* 2021;13:35818-35827.

25. Zhu Y, Zheng X, Zhang W, et al. Near-infrared-triggered nitrogen fixation over Upconversion nanoparticles assembled carbon nitride nanotubes with nitrogen vacancies. *ACS Appl. Mater. Interfaces.* 2021;13:32937-32947.

26. Mo Z, Zhu X, Jiang Z, et al. Porous nitrogen-rich g-C_3N_4 nanotubes for efficient photocatalytic CO_2 reduction. *Appl. Catal. B Environ.* 2019;256:117854.

27. Han C, Du L, Konarova M, Qi D, Phillips D, Xu J. Beyond hydrogen evolution: solar-driven, water-donating transfer hydrogenation over platinum/carbon nitride. *ACS Catal.* 2020;10:9227-9235.

28. Shen H, Choi C, Masa J, et al. Electrochemical ammonia synthesis: mechanistic understanding and catalyst design. *Chem.* 2021;7:1708-1754.

29. Hui X, Li L, Xia Q, et al. Interface engineered $Sb_2O_3/W_{18}O_{49}$ heterostructure for enhanced visible-light-driven photocatalytic N_2 reduction. *Chem. Eng. J.* 2022;438:135485.

30. Shen Z, Cheng M, Yuan Y, et al. Identifying the role of interface chemical bonds in activating charge transfer for enhanced photocatalytic nitrogen fixation of Ni_2P-black phosphorus photocatalysts. *Appl. Catal. B Environ.* 2021;295:120274.

31. Cheng L, Yin H, Cai C, Fan J, Xiang Q. Single Ni atoms anchored on porous few-layer g-C_3N_4 for photocatalytic CO_2 reduction: the role of edge confinement. *Small.* 2020;16:2002411.

32. Zhu X, Cao Y, Song Y, et al. Unique dual-sites boosting overall CO_2 Photoconversion by hierarchical electron harvesters. *Small.* 2021;2103796:2103796.

33. Liang Z, Zhuang X, Tang Z, Deng Q, Li H, Kang W. High-crystalline polymeric carbon nitride flake composed porous nanotubes with significantly improved photocatalytic water splitting activity: the optimal balance between crystallinity and surface area. *Chem. Eng. J.* 2022;432:134388.

34. Xu F, Mo Z, Yan J, et al. Nitrogen-rich graphitic carbon nitride nanotubes for photocatalytic hydrogen evolution with simultaneous contaminant degradation. *J. Colloid. Interface Sci.* 2020;560:555-564.

35. Lei G, Zhao W, Shen L, Liang S, Au C, Jiang L. Isolated iron sites embedded in graphitic carbon nitride (g-C_3N_4) for efficient oxidative desulfurization. *Appl. Catal. B Environ.* 2020;267:118663.

36. Feng C, Tang L, Deng Y, et al. Synthesis of leaf-vein-like g-C_3N_4 with tunable band structures and charge transfer properties for selective photocatalytic H_2O_2 evolution. *Adv. Funct. Mater.* 2020;30:2001922.

37. Kröger J, Jiménez-Solano A, Savasci G, et al. Interfacial engineering for improved Photocatalysis in a charge storing 2D carbon nitride: melamine functionalized poly(heptazine imide). *Adv. Energy Mater.* 2020;11:2003016.

38. Shi S, Sun Z, Bao C, Gao T, Hu Y. The special route toward conversion of methane to methanol on a fluffy metal-free carbon nitride photocatalyst in the presence of H_2O_2. *Int. J. Energy Res.* 2020;44:2740-2753.

39. Deng Y, Liu J, Huang Y, et al. Engineering the photocatalytic behaviors of g/C_3N_4-based metal-free materials for degradation of a representative antibiotic. *Adv. Funct. Mater.* 2020;30:2002353.

40. Chen Y, Yang M, Jia Y, et al. NiS_2/NiFe LDH/g-C_3N_4 ternary heterostructure-based label-free photoelectrochemical aptasensing for highly sensitive determination of enrofloxacin. *Mater. Today Chem.* 2022;24:100845.

41. Wang S, Zhao H, Zhao X, et al. Surface engineering of hollow carbon nitride microspheres for efficient photoredox catalysis. *Chem. Eng. J.* 2020;381:122593.

42. Zhang W, Peng Q, Shi L, et al. Merging single-atom-dispersed iron and graphitic carbon nitride to a joint electronic system for high-efficiency photocatalytic hydrogen evolution. *Small.* 2019;15:1905166.

43. Jiang Y, Liu Q, Tan K, Wang F, Ng H. Insights into mechanisms, kinetics and pathway of continuous visible-light photodegradation of PPCPs via porous g-C_3N_4 with highly dispersed Fe(III) active sites. *Chem. Eng. J.* 2021;423:130095.

44. Hayat A, Sohail M, Taha T, et al. Molecular grafting based polymeric carbon nitride for wondrous artificial photosynthesis. *Int. J. Energy Res* 2021;1-12:1882-1893.

45. Yao C, Wang R, Wang Z, Lei H, Dong X, He C. Highly dispersive and stable Fe^{3+} active sites on 2D graphitic carbon nitride nanosheets for efficient visible-light photocatalytic nitrogen fixation. *J. Mater. Chem. A.* 2019;7:27547-27559.

46. Liu Q, Chen C, Yuan K, et al. Robust route to highly porous graphitic carbon nitride microtubes with preferred adsorption ability via rational design of one-dimension supramolecular precursors for efficient photocatalytic CO_2 conversion. *Nano Energy.* 2020;77:105104.

47. Zhu X, Zhou G, Yi J, et al. Accelerated Photoreduction of CO_2 to CO over a stable Heterostructure with a seamless Interface. *ACS Appl. Mater. Interfaces.* 2021;13:39523-39532.

48. Yan P, Jin Y, Xu L, et al. Enhanced photoelectrochemical aptasensing triggered by nitrogen deficiency and cyano group simultaneously engineered 2D carbon nitride for sensitively monitoring atrazine. *Biosens. Bioelectron.* 2022;206:114144.

49. Zhu X, Yang J, Zhu X, et al. Exploring deep effects of atomic vacancies on activating CO_2 photoreduction via rationally designing indium oxide photocatalysts. *Chem. Eng. J.* 2021;422:129888.

50. Hayat A, Taha T, Alenad A, et al. A molecular amalgamation of carbon nitride polymer as emphasized photocatalytic performance. *Int. J. Energy Res.* 2021;45:19921-19928.

51. Shen H, Yang M, Hao L, Wang J, Strunk J, Sun Z. Photocatalytic nitrogen reduction to ammonia: insights into the role of defect engineering in photocatalysts. *Nano Res.* 2021;15:2773-2809.

52. Guo Y, Yang J, Wu D, et al. Au nanoparticle-embedded, nitrogen-deficient hollow mesoporous carbon nitride spheres for nitrogen photofixation. *J. Mater. Chem. A.* 2020;8:16218-16231.

SUPPORTING INFORMATION

Additional supporting information may be found in the online version of the article at the publisher's website.